Research Article

Ridwan Ridwan, Wahidin Nuriana, and Aditya Rio Prabowo*

Energy absorption behaviors of designed metallic square tubes under axial loading: Experiment-based benchmarking and finite element calculation

https://doi.org/10.1515/jmbm-2022-0052
received May 01, 2022; accepted June 22, 2022

Abstract: In this article, the load resistance and energy absorptions of thin-walled structures on the square tube were numerically evaluated by the finite element method. This structure can be widely used in automotive industries, industrial buildings, ships, offshore platforms, and airplanes. In the finite element method, thin-walled structures on square tubes were examined with different wall thicknesses and materials. The materials used are mild steel, SAE 1045 steel, and SAE 1008 steel. Using the numerical results, the thickness of the wall influences the strength of the structure. Moreover, SAE 1045 steel material also seems to increase the strength of the tube under axial loading compared to the mild steel and SAE 1008 steel material. It is also important to remember that the finite element solution depends on defining your mesh size and boundary conditions. The mesh size is also compared and assessed.

Keywords: axial load, thin-walled structure, energy absorption, square tubes, wall thickness, carbon steel

1 Introduction

Thin-walled structures comprise an important proportion of construction engineering and are continuously being developed till date. This construction application is also very diverse, ranging from those used on land, *e.g.*, automotive industries, industrial buildings [1,2]; at sea, *e.g.*, ships, offshore platforms [3–6]; and even in the air such as airplanes [7]. This construction application in society can include individuals and even many people at once. For instance, ship and airplane transportation is used by many people as a medium to move from one island to another and as a transporter of goods. Therefore, the aspect of transportation safety is very important for the wider community.

In the last two decades, research and development of energy absorbers to reduce effects on humans and structures has become an interesting topic for researchers. For instance, the material properties of a square tube under axial explosive loading play an important role in the formation of the buckling pattern, which has been experimentally investigated by Karagiozova *et al.* [8]. Furthermore, the effect of different shapes of the hollow tube also appears to play an important role in energy-absorbing as in the research carried out by Marzbanrad *et al.* [9]. The research showed that the ellipse cross-section had more energy absorption compared to the square and circular cross-sections. In the same year, research on the effect of geometrical parameters, *i.e.*, square, hexagonal, and conical, on the energy absorption characteristics of thin-walled structures has been performed by Guler *et al.* [10]. It was noted in the research that the conical geometry was the most efficient to absorb the energy during the axial impact loading. A year afterward, a new design that is efficient in improving crashworthiness characteristics of cylinder tubes, *e.g.*, sensitivity to external loading, crushing stability, crush force efficiency, and collapse mode while subjecting to axial impact loading, has been introduced by Salehghaffari *et al.* [11]. The method used by Salehghaffari *et al.* [11] was attachment of an expanding ring to the cylinder wall. However, this optimized design applies only to low-velocity loading, because high-velocity loading seems to have a difference in energy absorber for tubes under axial loading [12]. Not only experiments but

* **Corresponding author: Aditya Rio Prabowo,** Department of Mechanical Engineering, Universitas Sebelas Maret, Surakarta 57126, Indonesia, e-mail: aditya@ft.uns.ac.id
Ridwan Ridwan, Wahidin Nuriana: Department of Mechanical Engineering, Universitas Merdeka Madiun, Madiun 63133, Indonesia

also numerical computational approaches such as finite element method are also important for simulating tubes under axial loading, and their outcomes are quite good compared to the direct experiments in terms of energy absorbed [13,14].

The present article deals with a numerical study of the thin-walled structure of hollow tubes with different thickness walls when subjected to axial impact loading. The finite element method, which is one of the numerical problem-solving techniques, will be employed to calculate the issue of the tube under axial loading. This experiment will be a reference to determine the parameter's capability to absorb energy, load *versus* displacement curve, and mode deformation. Influence of the material properties of the tube on their modes of energy absorption is also discussed. Furthermore, the finite element models of the tube with different mesh sizes will be analyzed and the calculated results will be compared. Benchmarks are also carried out based on an experiment to ensure the results are reliable.

2 Methods

2.1 Benchmark details

The thin-walled structure of the square tube in the axial loading experiment conducted by Abdullah *et al.* [15] is the benchmark in this study. This benchmark is carried out for legitimized assurance of the validity of the study. The experimental setup was carried out with SHIMADZU Universal Testing Machine. The steel press head (impactor) is positioned directly above the specimen. Meanwhile, the stationary support is positioned on the bottom of the specimen. From this previous axial loading experiment, a square tube specimen with a similar cross-sectional geometry was used in the current consideration. It had been determined that the test specimens were symmetric thin-walled square tube with a dimension of 38 mm × 38 mm and a thickness of 1.2 mm. The overall length of the specimen is approximately 95 mm calculated from the top end of the specimen to the bottom of the specimen that is towed with a stationary support. The axial loading step was carried out by compressing the specimen with a steel press head to until 47.5 mm downward. The detailed experiment scheme is shown in Figure 1a. The load *versus* displacement curve will be compiled by monitoring the forces and displacements on the specimen during axial loading.

The experimented specimen was constructed with the aluminum material. This material is widely used for components in the transportation, aerospace, and also included in construction industries. Moreover, these aluminum materials are known for excellent mechanical properties such as lightweight, durability, malleability, and corrosion resistance. Selection of this material also takes into account that the characteristics to be machined and cast are immensely easy. The aluminum material in square tube has a density ρ of 2,700 kg/cm^3, a Young's modulus E of 68 GPa, and a Poisson's ratio υ of 0.33 (Table 1).

The nonlinear finite element analysis (NLFEA) is conducted using ANSYS LS-DYNA [16]. Specimen configuration with an upper head press and a mesh size that has been applied is shown in Figure 1b. A mesh convergence study to determine the magnitude of the error compared

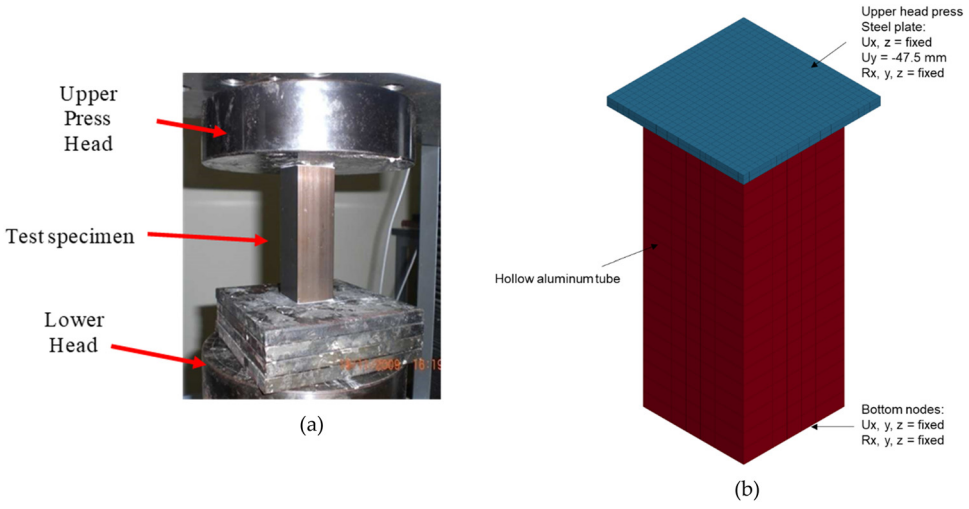

Figure 1: (a) Experiment scheme of the hollow tube under axial loading [15]. (b) Discretized specimen in finite element modeling.

Table 1: Material properties for the aluminum

Material	Density ρ (kg/cm³)	Young's modulus E (GPa)	Poisson's ratio υ (–)
Aluminum	2,700	68	0.33

to the experiment was also carried out with mesh sizes of 1, 3, and 5 mm. For the specimen, the mesh is made with the shell element type. For the press, it uses a solid element type.

The comparison of the load *versus* displacement curve from the experiment and the finite element method of thin-walled tube under axial loading is shown in Figure 2. It can be seen that the numerical method gives quite satisfactory results. The maximum forces for mesh sizes of 1, 3, and 5 mm produce peaks of 27.9, 29.39, and 29.39 kN, respectively, compared to the experiment where the peak maximum force was 31.14 kN. The largest difference in maximum force is the result when a mesh size of 1 mm is used, with an error of about 10.4%. On the other hand, for the mesh size of 3 and 5 mm, the error tends to be less, which is around 5.6% compared to the experiment. Furthermore, the collapse behavior of the tubes is presented in Figure 3. Viewed from two sides, namely the side and the top for the numerical method, the results are quite good in terms of the collapse behavior of the tubes. The upper part of the tube that is in contact with the upper head press experiences a lot of plastic deformation which is indicated by the folding on this side. The lower side, which is the support side, does not look much changed and still shows its original shape which is a square. The two analyses of load *versus* displacement and collapse behavior show that the numerical method specifically the finite element method can be relied on for the results for simulating thin-walled tubes under axial loading.

One of the tests that are often used to determine the properties of a material is the tensile test. In addition, many studies on this tensile test are even used as a tool to test a failure criterion, *i.e.*, ship damage modeling using the finite element method [18–21]. The tensile test experiment conducted by Cabezas and Celentano [17] will be reconducted using the finite element method. Figure 4a shows the dimensions of the specimen, and Figure 4b shows the specimen in the finite element method. The overall length of the specimen is 200 mm, which has a length of the fault area measuring 60 mm with a width of 12.5 mm. The width and length of the grip sections measure 20 and 50 mm, respectively. The thickness of the specimen is 6 mm. The material selected is SAE 1045 steel, which has a density ρ of 7,870 kg/cm^3, an E modulus of elasticity of 206 GPa, and a Poisson's ratio of 0.29. To obtain the stress *versus* strain value, the following equations are considered:

$$\sigma = \frac{F}{A_0}, \tag{1}$$

$$\varepsilon = \frac{\Delta L}{l_0}, \tag{2}$$

where σ is the stress and ε is the strain. F is the applied load, A_0 is the cross-sectional area of the specimen, Δl is the elongation, and l_0 is the original length.

The comparison of stress *versus* strain taken from the experiment and the finite element is shown in Figure 5. It can be seen that the stress results obtained through numerical simulations are similar to the experimental data. The maximum stress of 765.9, 765.9, 765.9, 765.9,

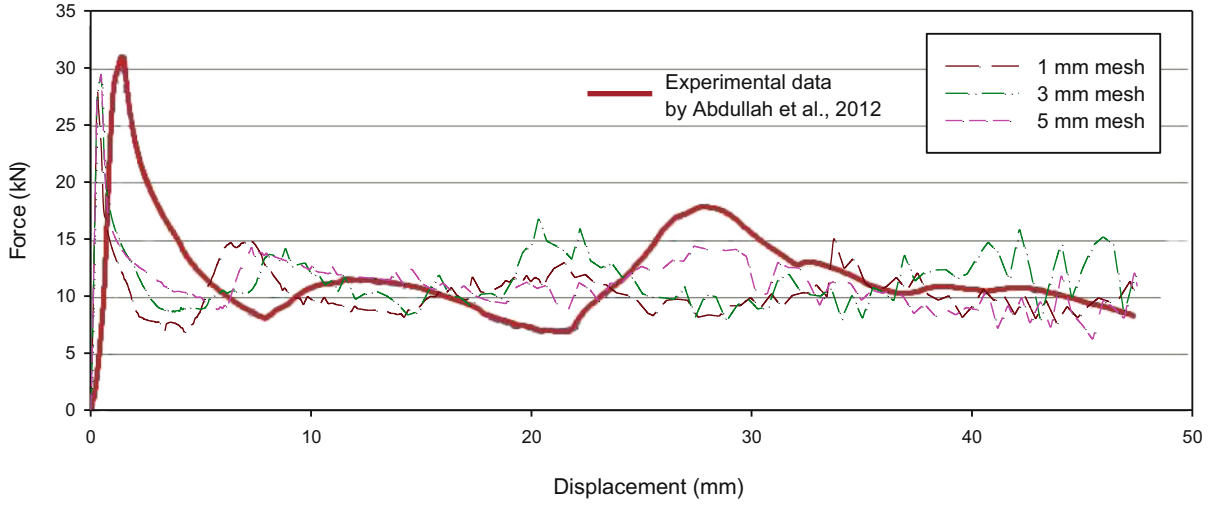

Figure 2: Comparison of the force *versus* displacement curve between experimental data and FEA.

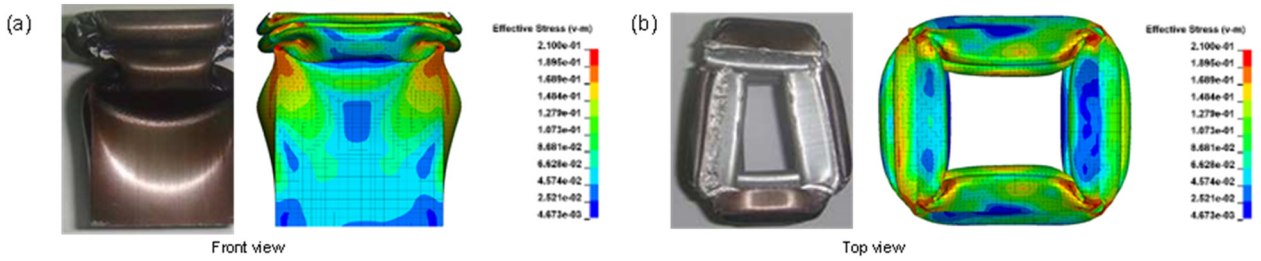

Figure 3: Comparison results between experiment and finite element of the tube under axial loading: (a) front view and (b) top view.

and 766 MPa resulted from mesh sizes of 1, 2, 3, 4, and 5 mm, respectively. The maximum stress from the experimental data is 762 MPa. This condition gives an error value that tends to be small, not more than 0.5%. As for the comparison at the yield stress point, the highest error percentage is 3.4% when the mesh size is 3 mm. The yield stress values are 450.9, 450.9, 467, 454.5, and 460.7 MPa for mesh sizes of 1, 2, 3, 4, and 5 mm, respectively. The experiment itself is 451.6 MPa. The ratio between the experiment and the numerical simulation is shown in Figure 6. Figure 7 shows the fracture in a specimen whose fracture accuracy is quite similar to that of the experiment. Unique phenomena such as localized necking are also very visible near the fault. However, the fracture point is slightly different where the fault that occurs in the finite element is slightly closer to the grip section, while in the experiment it occurs in the middle of the gauge length. Overall, the numerical method has a good agreement with the experiment.

2.2 Finite element configuration and boundary condition

Finite element configuration is made to describe tubes under axial loading. This configuration is based on previous experiments [15]. The specimen dimensions of the tube are shown in Figure 8. The overall length and width are 95 and 38 mm, respectively. Three thickness variations with sizes of 2, 3, and 4 mm were proposed for further comparison. Details of the specimen and tube wall thickness are shown in Figure 8.

The boundary condition scheme for numerical simulation of a loaded tube is shown in Figure 9. At the top of the specimen, which is 95 mm from the bottom of the specimen, there is a box-shaped press with dimensions of 50 mm × 50 mm and a thickness of 3 mm. This press will press down on the y-axis with a speed of $v = 0.5$ m/s until it reaches 47.5 mm. The translational constraints and rotational constraints are made in Ux and Uz equal to fixed, and Rx, y, z equal to fixed, respectively. The box press is made with the solid element, and using the steel material with a density ρ of 7,860 kg/m^3, a Young's modulus E of 206 GPa, and a Poisson's ratio ν of 0.29. As for the specimen, it is made using a shell element type (Figure 8). The shell element is created with the element formulation option with number 16 whereas ANSYS LS-DYNA is the code for the fully integrated shell element-type element. The selection of this element formulation option is due to that this option can generate fast simulation and reduce the simulation time. For the shear factor, the value that has been used is 0.83. There are shell analysis approaches that have been proposed by researchers, such as in the literature [22–25] to calculate an account for large deformations options. The first two approaches are based on isogeometric analysis and have advantages in this aspect; also, in dynamics while the last approach entirely uses deep neural networks and avoids a finite element

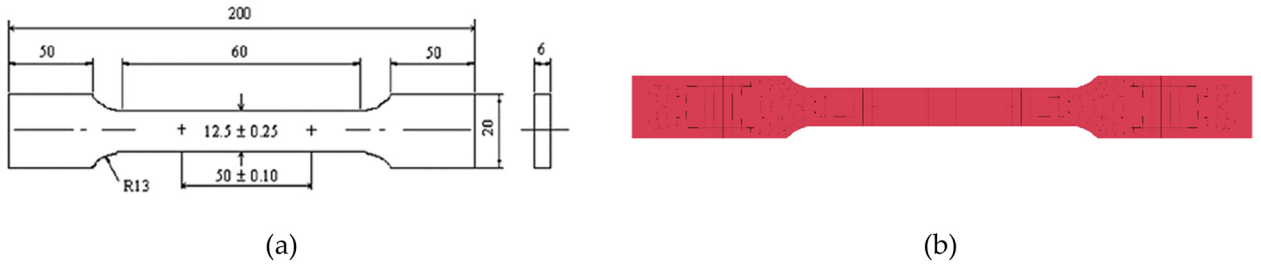

Figure 4: (a) Dimension of the tensile test specimen [17]. (b) Finite element of the specimen.

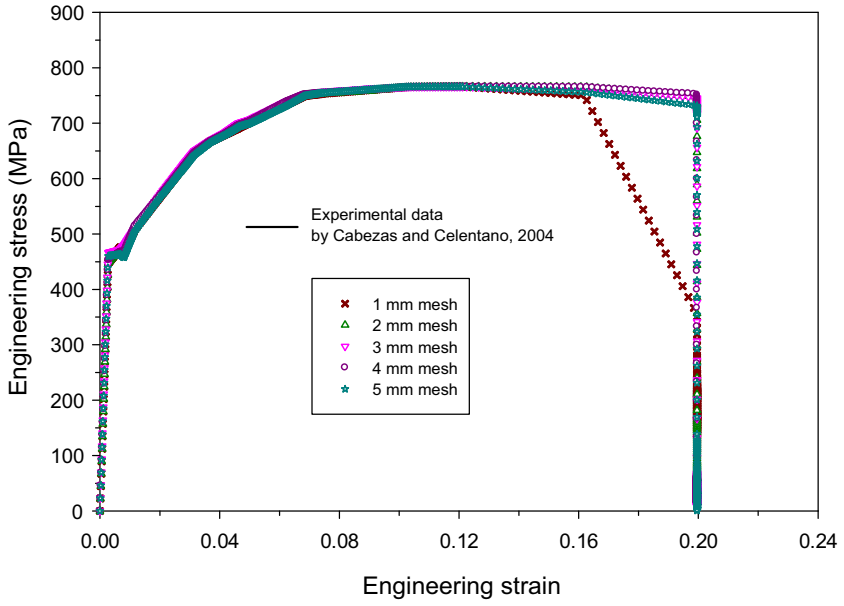

Figure 5: Comparison of the engineering stress engineering *versus* strain between experimental data [17] and finite element method.

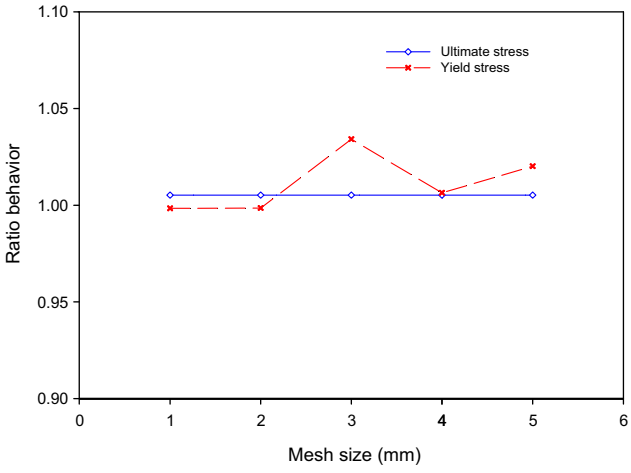

Figure 6: Ratio stress between experiment and finite element method.

discretization. The bottom of the specimen is stationary support with displacement and rotation made to *Ux*, *y*, *z* = fixed, and *Rx*, *y*, *z* = fixed, respectively. The simulation is carried out for 1 s from the beginning of pressing to the final result.

Despite the element formulation number 16, ANSYS LS-DYNA also includes the shell element formulation, *i.e.*, Belytschko–Tsay shell element formulation [26,27]. By default, the Belytschko–Tsay shell element formulation option is found in number 2 ANSYS LS-DYNA. This shell method is usually for non-linear dynamic fracture and arbitrary evolving cracks. A fully integrated version of this shell was implemented by suitably modifying element type number 16.

In ANSYS LS-DYNA user-defined material model [16], there is a constitutive model and certain material input parameters that are considered in this study. The first to be implemented in a user-defined material model is the element failure routine material 024. Material 024 is a piecewise linear plasticity model that utilizes the material behavior defined in Figure 10. The engineering stress for a given strain becomes the primary input data for influencing the area of elasticity and plasticity of the material. For each value of yield stress, each strain is arranged to zero. The next primary input parameters are the material properties such as density ρ, Young's modulus E, Poisson's ratio υ, and failure strain ε_f. In the second user-defined material model which is for the box-shaped press, material 020 is used. Material 020 is rigid, where the input parameters given are limited to density, Young's modulus, and Poisson's ratio. The relationship between engineering stress *versus* engineering strain is negligible in this material model.

The proposed materials are compiled in Table 2 along with their material properties. Aluminum material was used to determine the effect of tube wall thickness on the load-bearing strength. Aluminum has a property density ρ of 2,700 kg/cm^3 and a Young's modulus E of 68 GPa. The materials used are mild steel, SAE 1045 steel, and SAE 1008 steel. Mild steel has a property density ρ of 7,850 kg/cm^3, a Young's modulus E of 201 GPa, and a Poisson's ratio of 0.3. As for SAE 1045 steel, the material has a density property ρ of 7,800 kg/cm^3, a Young's modulus E of 205 GPa, and a Poisson's ratio of 0.3. SAE 1008

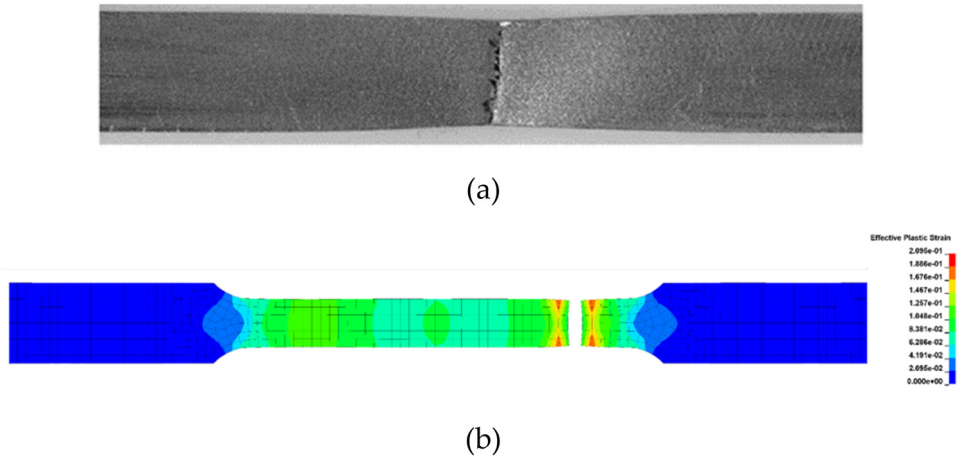

Figure 7: Fracture on the tensile test specimen. (a) Experimental data [17]. (b) Finite element method.

steel has a property density ρ of 7,870 kg/cm^3, a Young's modulus E of 206 GPa, and a Poisson's ratio of 0.29. Meanwhile, to determine the effect of material on the specimen tube under axial loading, the thickness of the tube is set at 2 mm only.

The choice of steel material is due to the many needs for engineering applications using steel materials. Many means of transportation use steel as the primary choice. For mild steel material itself, it is one type of carbon steel that contains a low level of carbon. The characteristics of mild steel are high tensile and impact resistance, as well as good ductility and weldability. This mild steel material can be applied to one of the plates on the ship when grounding damage occurs [28]. However, the most widely used material for offshore structures is steel with ASTM code A-36 [29]. SAE 1045 steel is a type of carbon steel that contains a medium amount of carbon in its composition. SAE 1045 steel is commonly found in the construction and automotive industries [30]. It is widely used in industrial applications that demand higher wear resistance and strength. Typical applications in which SAE 1045 steel is used contain die forging, hot upsetting,

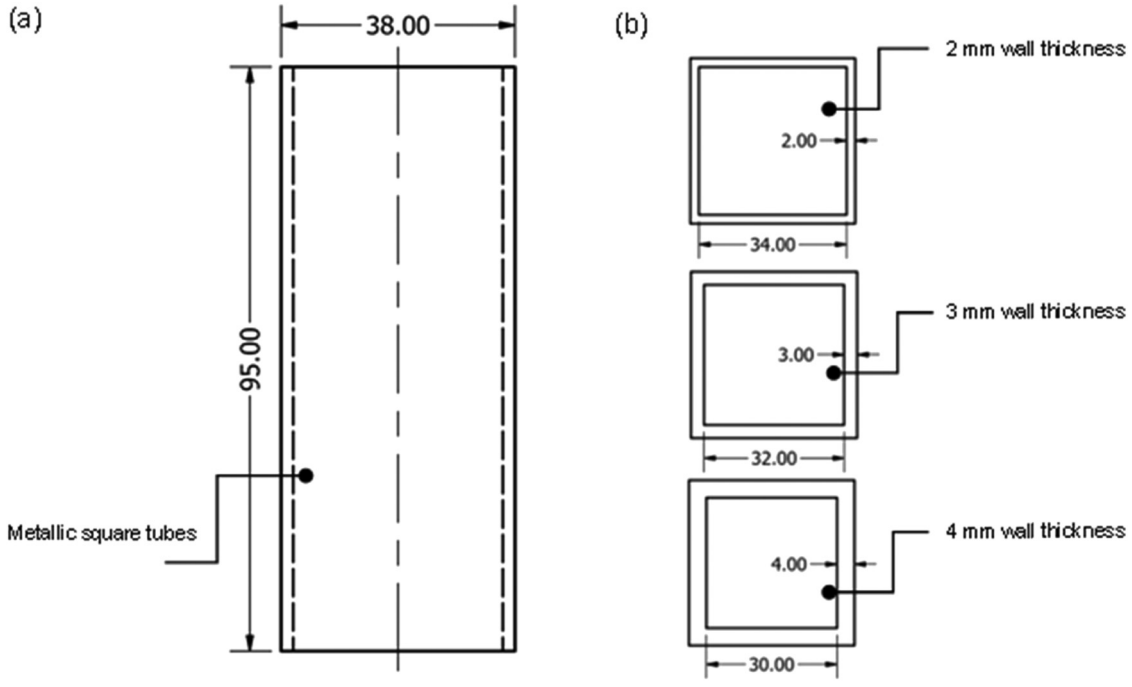

Figure 8: (a) Dimension of the tube. (b) Dimension of the wall thickness.

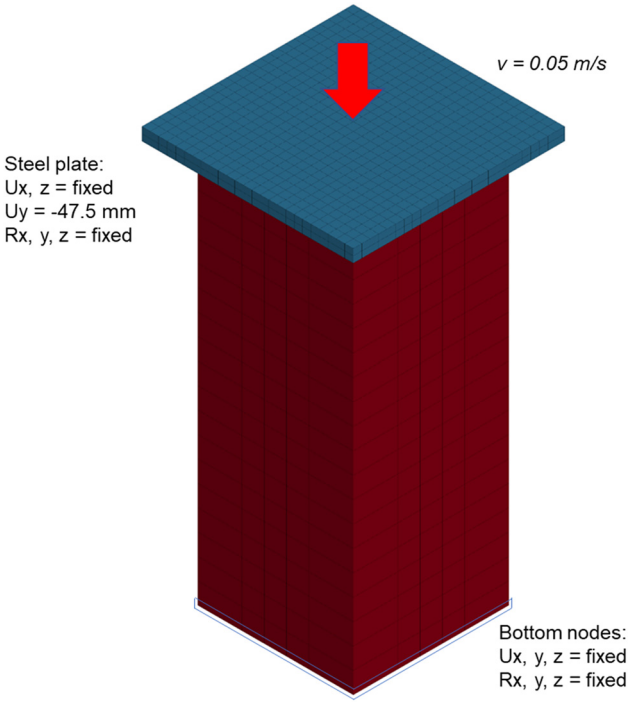

Figure 9: Finite element configuration and boundary condition.

and machinery parts. Some materials which are equivalent to SAE 1045 steel are ASTM A568 Grade 1,043 and also ASTM A576 Grade G10430. The material SAE 1008 steel is a type of carbon steel that contains a low level of carbon. It is mainly used in extruded, cold upset, cold-headed, and cold pressed parts and forms. Some materials which are equivalent to SAE 1045 steel are ASTM A512 Grade 1008 and ASTM A513 Grade 1008.

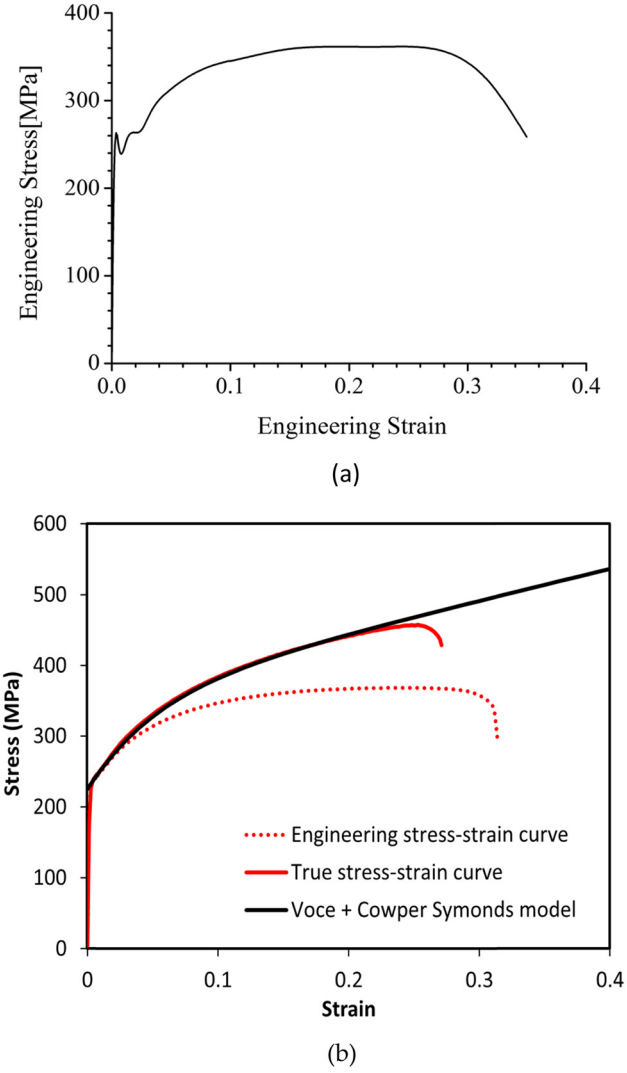

Figure 10: The engineering stress *versus* engineering strain. (a) Mild steel [31] and (b) SAE 1008 carbon steel [20].

3 Results and discussion

3.1 Effect of thickness change

The load *versus* displacement curve is described as the load-bearing ability of the square tubes when they are crushed under axial load. Here, the corresponding load *versus* displacement curve for three different wall thicknesses of the tube under axial loading is presented in Figure 11. It can be seen that the tube wall thickness greatly affects the acting force. The thickness of 4 mm seems to provide greater resistance to axial loads compared to tube wall thicknesses of 2 and 3 mm. The first area on this graph is linear to the maximum force which then decreases. The maximum force for a tube with a wall thickness of 2 mm is 51.9 kN. Meanwhile, the wall thicknesses of 3 and 4 mm gave values of 80.2 and 109.5 kN, respectively. In fact, it shows that the resistance to axial load increases by 54.53% from 2 to 3 mm thickness, and increases by 36.53% from 3 to 4 mm wall thickness (Figure 12).

A comparison between the relating energy *versus* displacement curves of these specimens is presented in Figure 13. As it is shown, the increase in the thickness of the square tube wall can increase the absorbed energy caused by the axial loading. Furthermore, a specimen with a wall thickness of 4 mm takes immensely more energy than specimens with 2 and 3 mm wall thickness during axial loading tests. In specimen with 2 mm wall thickness, the total energy absorbed resulted to be 1296.6 J, and it takes less energy compared to specimens with 3 and 4 mm wall

Table 2: Material properties of steel

Material	Density ρ (kg/m^3)	Young's modulus E (GPa)	Poisson's ratio υ (–)
Mild steel	7,850	201	0.3
SAE 1008 carbon steel	7,800	205	0.3
SAE 1045 steel	7,870	206	0.29

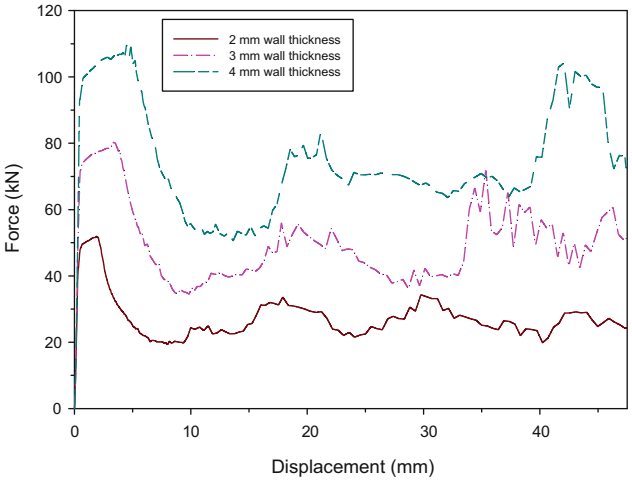

Figure 11: Force *versus* displacement curve generated during axial loading with three different wall thicknesses.

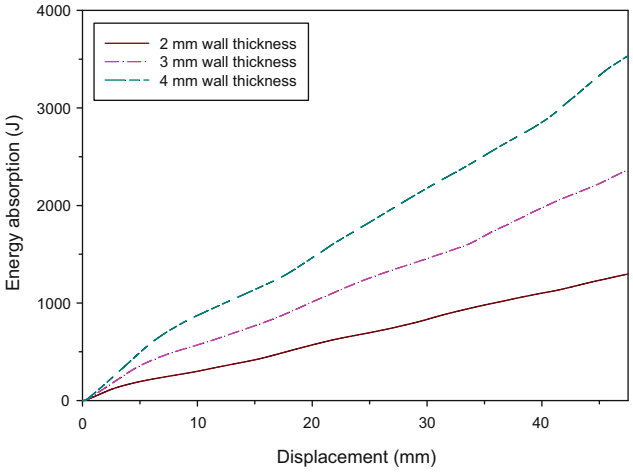

Figure 13: Energy absorption generated during axial loading with three different wall thicknesses.

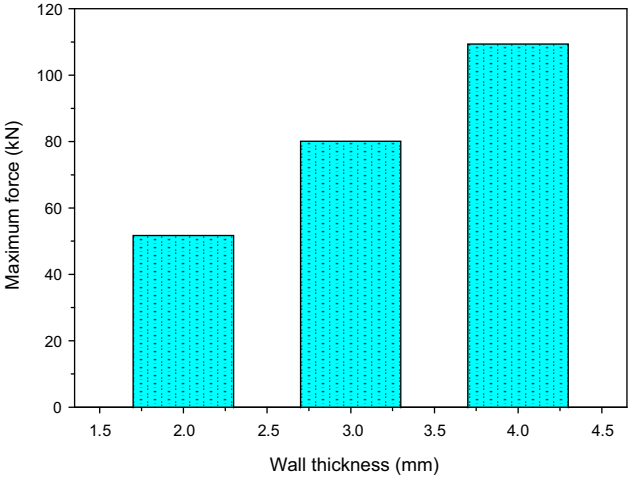

Figure 12: The maximum force generated during axial loading with three different wall thicknesses.

thickness. Specimens with 3 and 4 mm thickness have absorbed the energy of 2364.4 and 3534.6 J at the final end simulation, respectively. There was an 82.35% increase in absorbed energy for a 2 mm wall thickness to 3 mm wall thickness specimen and a 49.49% increase for a 3–4 mm thickness specimen. It indicates that the higher value of energy absorbed belongs to a 4 mm wall thickness specimen.

In Figures 14 and 15, the wall thickness variations of the square tube with a size of 2, 3, and 4 mm with von-Mises stress contour and strain contour are shown. The results indicate that differences in the thickness of the tube wall when subjected to axial loading affect the collapse mode of deformation. Figures 13 and 14 show that both specimens with 2 and 3 mm wall thickness present a folding collapse behavior on top of the tube compared to the 4 mm wall thickness that seems to hold the folding collapse at the end simulation. Several folding petals and snap-back damage modes were also presented after the axial loading. These phenomena can be seen in the crushed shape of all specimens at time = 1 s (Figures 14 and 15).

The remarkable difference between these three thickness variations is seen at the end of the simulation where time = 1. Large stress is formed in the folding and below the folding section area. The distribution of von-Mises stress is seen more in the tube with a thickness of 4 mm, as shown in Figure 14, which indicates a lot of red in this area. Furthermore, the bottom is just below the fold as a result of the load experiencing great stress. This excess stress is seen as long as from t = 0.20, t = 60 until the end of loading is complete. The smaller the size of the wall thickness, the less area that can withstand

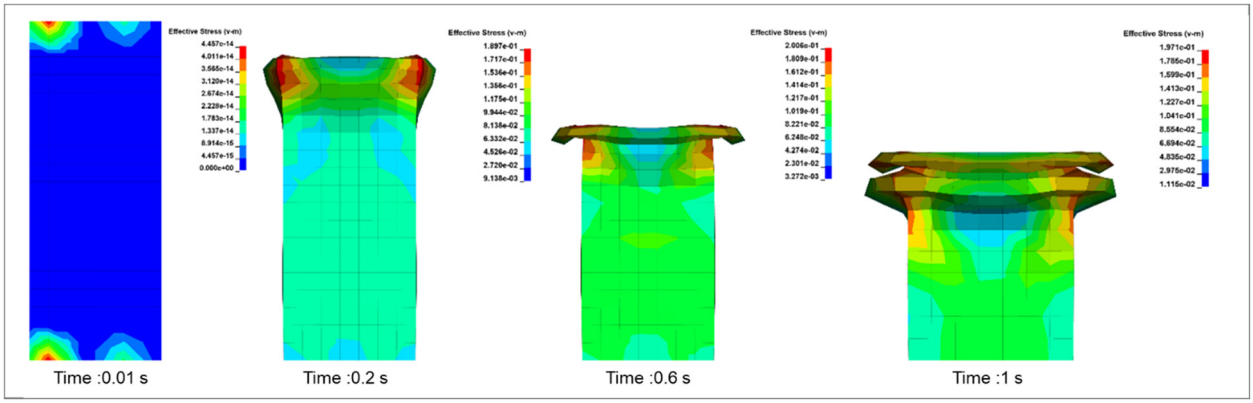

(a)

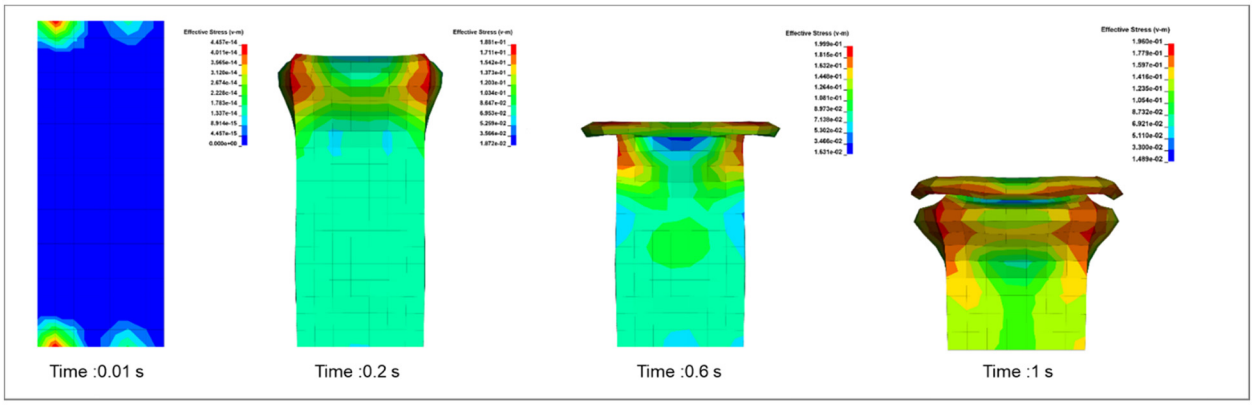

(b)

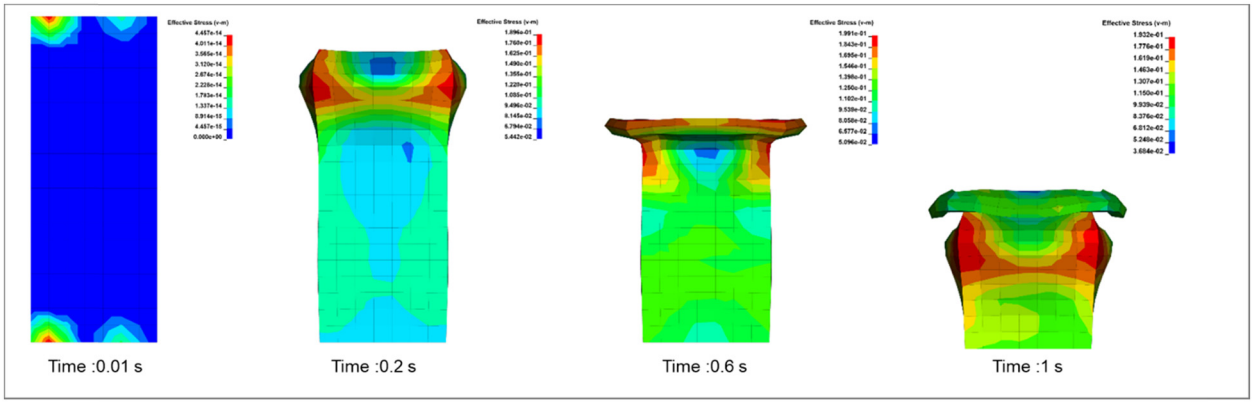

(c)

Figure 14: Distribution of the von-Mises stress on the specimen scaling the time from 0.01 to 1 s. (a) 2 mm wall thickness, (b) 3 mm wall thickness, and (c) 4 mm wall thickness.

stress. However, the stress value did not show significantly different results. This was seen when the final specimens had stresses at 197, 196, and 193, for the 2, 3, and 4 mm specimens, respectively. Numerical results indicate that the thickness of the square tube has an effect on their collapse mode of deformation.

The wall thickness of 2 mm provides a very visible folding and decreases less as the wall thickness increases. Some similarities seem to appear between the proposed wall thicknesses. When the loading begins to take place or $t = 0.01$ s, the stress distribution shows the same location, namely the part close to the plate under load and the

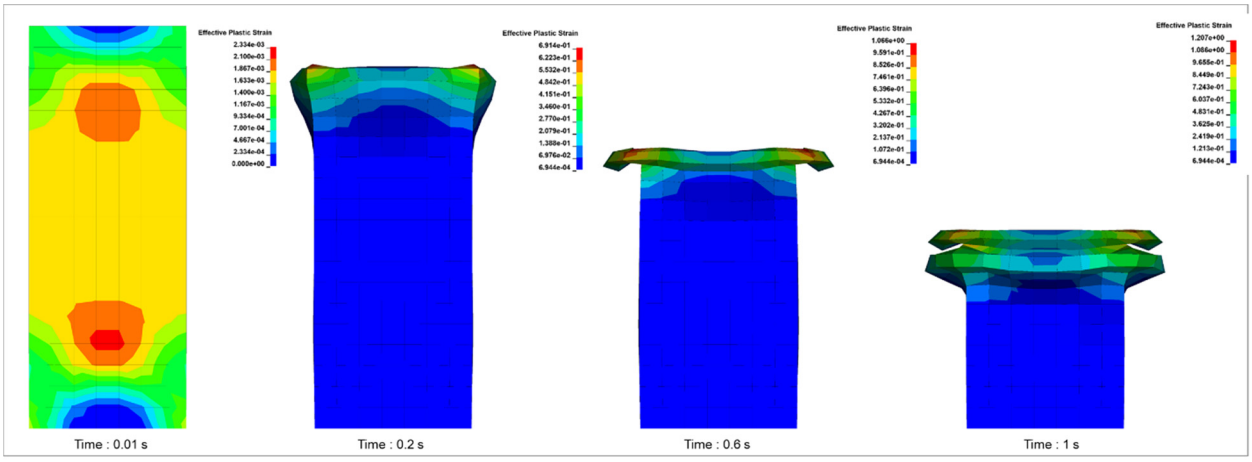

(a)

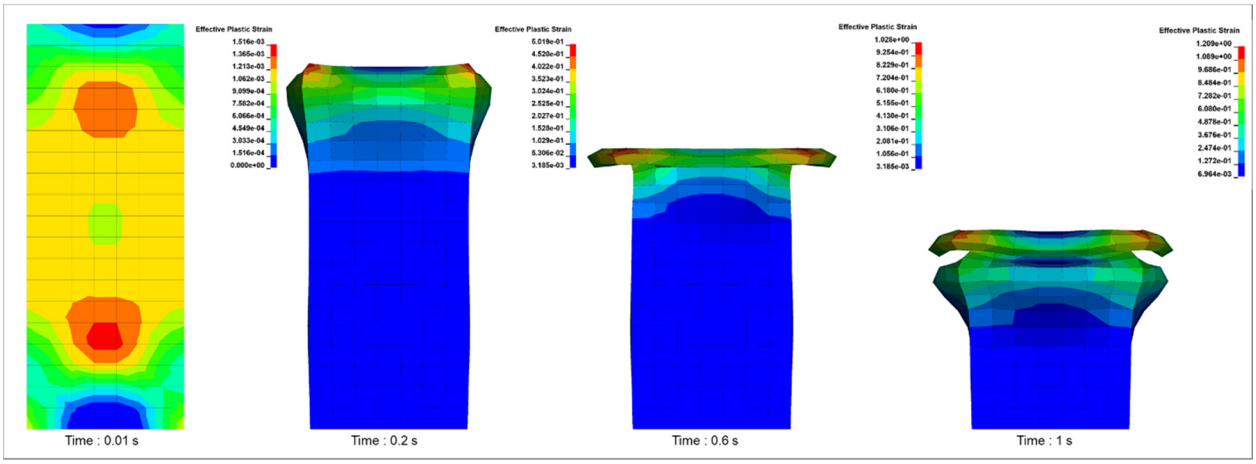

(b)

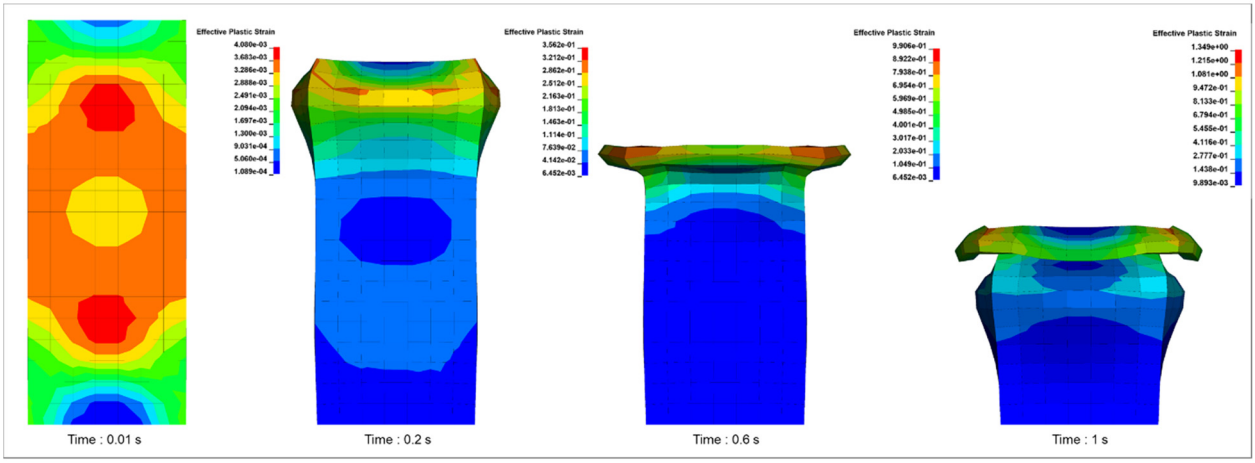

(c)

Figure 15: Distribution of the strain on the specimen scaling the time from 0.01 to 1 s. (a) 2 mm wall thickness, (b) 3 mm wall thickness, and (c) 4 mm wall thickness.

stationary support. The formation of stress occurs starting from the corners of the square tube which then spreads throughout the body tube.

The strain distribution also showed the same strain distribution between tubes with 2 mm thickness with 3 and 4 mm thickness. But the difference in the folding form began to be seen between the time $t = 0.20$ s and $t = 1$ s. The 2 mm thickness is easier to experience the folding phenomenon compared to 3 and 4 mm thickness. For the formation, the last folding, 4 mm thickness strengthens the wall quite bites as shown by the larger stress concentration, compared to the 2 and 3 mm, which experienced full and partial folding, respectively. The folding phenomenon seems to be influenced by the thickness of the tube wall.

3.2 Effect of material change

The load *versus* displacement curve obtained from the square tube under axial loading is presented in Figure 16. The materials used in the specimens were mild steel, SAE 1045 steel, and SAE 1008 steel. As it is seen, numerical results show that the given material on the tube, especially SAE 1045 steel, can affect significantly the load *versus* displacement curve while subjected to axial compression. Compared to mild steel and SAE 1008 steel, the load *versus* displacement graph is located below the graph produced by SAE 1045 steel material. These results show that using SAE 1045 steel material within specimens can increase the capability of withstanding the load produced by the axial loading. However, the results are not that much different from mild steel and SAE 1008 steel. This case shows that the material provides almost the same axial load-bearing strength. There is no significant difference that can be seen in the load *versus* displacement graph. In fact, this similarity occurs from the beginning of the load pressing the specimen until a displacement of 47.5 mm occurs or at the end of the simulation.

The material change also seems to affect the maximum force generated during the initial axial loading. A comparison between the maximum force on each material (mild steel, SAE 1045 steel, and SAE 1008 steel) is shown in Figure 16. It can be seen that specimens with SAE 1045 steel material have a maximum force higher compared to the mild steel and SAE 1008 steel material. It has a peak at approximately 161.8 kN compared with 80.3 and 80.7 kN, respectively. As a matter of fact, SAE 1045 material increases the amount of maximum force by 101.49 and 100.49% compared to the mild steel and SAE 1008 material. The graph in Figure 17 also shows that specimens with the mild steel and SAE 1008 steel are quite equal in providing maximum force in this case of the tube under axial loading. The difference between the two is very small at 0.4 kN or the percentage difference is only approximately 0.4%.

A comparison between the relating energy *versus* displacement curves of the specimens within material change is presented in Figure 18. As it can be seen from Figure 18, a specimen with the SAE 1045 tube can increase the absorbed energy produced by the axial loading, compared to the specimen with mild steel and SAE 1008 steel material. These results show that changing the material in

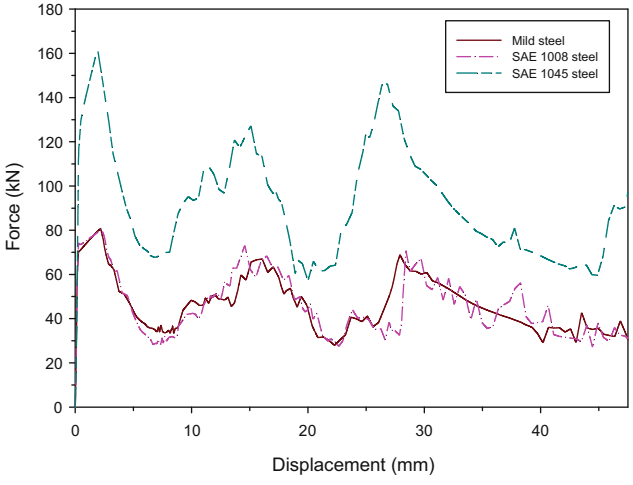

Figure 16: Force *versus* displacement generated during axial loading curve for three steel materials.

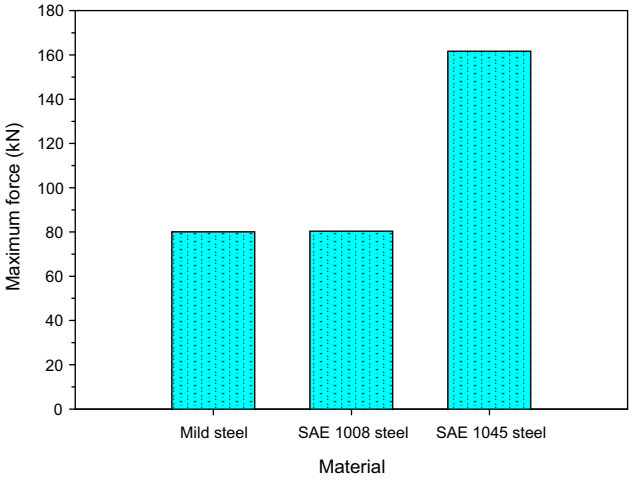

Figure 17: The maximum force generated during axial loading for three steel materials.

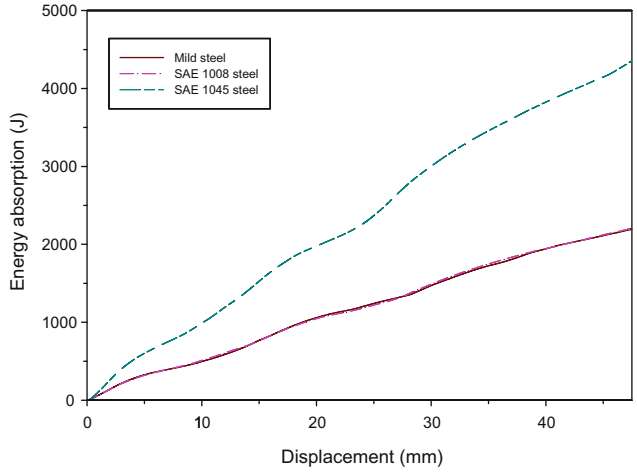

Figure 18: Energy absorption generated during axial loading with three steel materials.

the square tube affects the absorbed energy during the axial loading. Both mild steel and SAE 1008 steel material do not seem to have much difference in the capability of dissipating energy. The total energy absorbed from the SAE 1045 material tube is approximately 4355.4 J, which is much higher compared to the mild steel and SAE 1008 steel material, which is 2193.3 and 2205.5 J, respectively. This indicates that there is an increase in the total energy absorbed in the square tube with the SAE 1045 steel material by 98.58 and 97.48%, respectively, which is almost double the SAE 1045 steel material value.

Folding petals and snap-back damage modes of the square tube after the axial loading within mild steel, SAE 1045 steel, and SAE 1008 steel material are presented in Figures 19 and 20. The significant folding formation seems to be present on the specimens at the end of the simulation in three different materials. In fact, all these folding formations are plastic deformations which indicate that the applied load has passed the yield point in these materials. The tube wall is severely deformed inward and outward when viewed from the initial tube wall as is shown in the front and top view in Figures 19 and 20. Thus, these numerical results indicate that differences in the materials of the square tube can affect the collapse modes of deformation.

The distribution of the von-Mises stress contour on the specimen with the mild steel, SAE 1045 steel, and SAE 1008 steel material at the end of the axial loading is presented in Figure 18. A quite higher von-Mises stress seems presented under the last folding formation of the specimens. However, the stress that is quite obvious occurs at the elbow parts when the square tube uses SAE 1045 steel material which is located just below the last folding of the tube wall. It is observed that this region experiences stress of 693 MPa after loading was completed. Both mild steel and SAE 1008 steel also feel considerable stress in the elbow area of the tube wall. Compared to SAE 1045 steel material, the perceived stress is quite small at 292 and 334 MPa, respectively. This phenomenon shows that the specimen within SAE 1045 steel

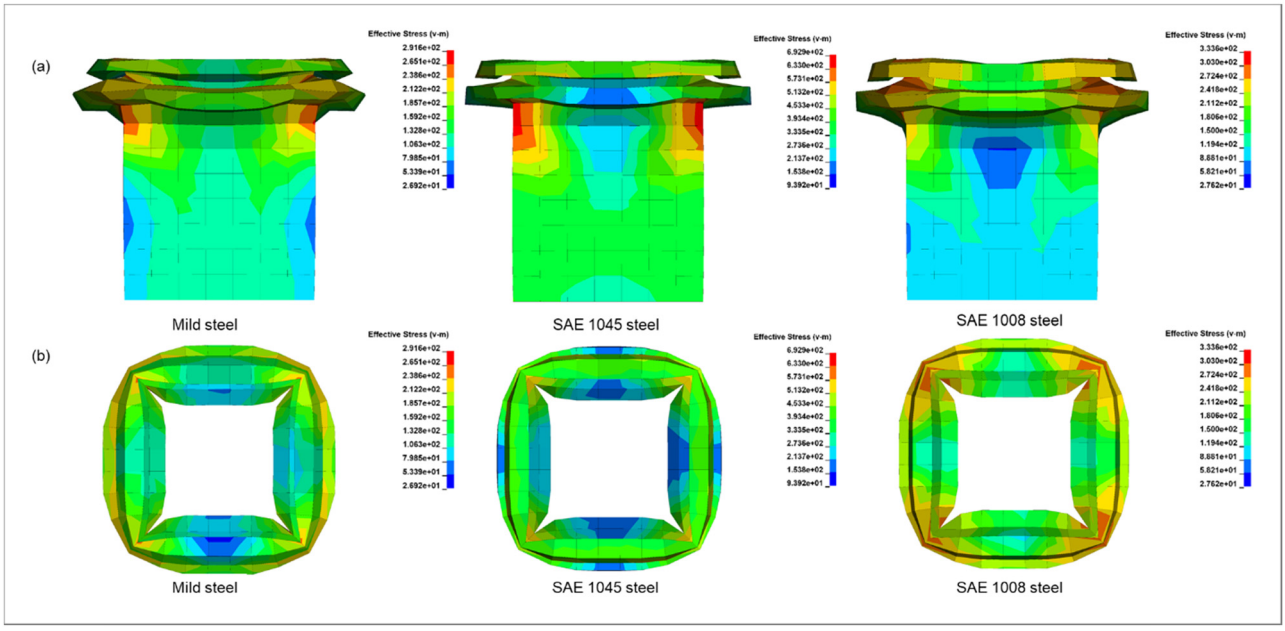

Figure 19: Distribution of the von-Mises stress on the specimen scaling the time from 0.01 to 1 s. (a) Side view and (b) top view.

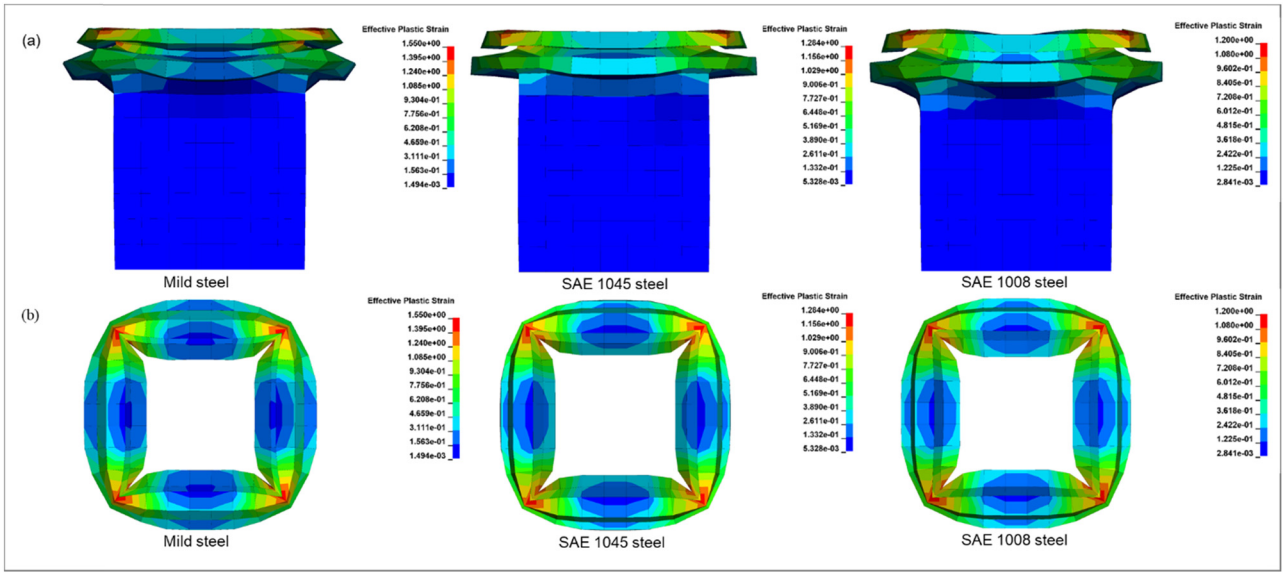

Figure 20: Distribution of the strain on the specimen scaling the time from 0.01 to 1 s. (a) Side view and (b) top view.

material has a higher stress experience approximately 137.33 and 107.49% compared to the specimens with the mild steel and SAE 1008 steel material.

The distribution of strains of specimens with mild steel, SAE 1045 steel, and SAE 1008 steel is shown in Figure 19. The strain is mostly felt in the folding section of the tube. In SAE 1045 steel material, the plastic strain shows a value of 0.13, which is right at the top of the tube when the first folding occurs. This can be seen after the simulation is completed and also felt by all specimens with this material. The numerical results for the mild steel and SAE 1008 steel material produce a plastic strain of 0.16 and 0.12, respectively. All three materials seem to give different plastic strain values. The effect of the selection of the material on the tube seems to cause differences in the plastic strain formation.

3.3 Mesh-dependent study

As it is known that the specimen tube when using FEA will be divided into small parts called mesh, meshing is one of the most important steps in performing an accurate simulation using FEA. A mesh is made up of elements that contain nodes (coordinate locations in space that can vary by element type) that represent the shape of the geometry. A mesh is made up of elements and an element is designed so that it can be solved for various quantities important to the problem at hand. Those elements connect all characteristic points (called Nodes) that lie on their circumference.

Figure 21 shows the load *versus* displacement in the case of different wall thicknesses with 3 mesh sizes, namely 2, 5, and 8 mm. As seen the mesh affects the results of the load *versus* displacement graph. It can be seen that if the mesh size increases, the overall graph looks increasingly shifted to the right which shows the greater the displacement. The maximum force on a square tube with 2 mm wall thickness is at a displacement of 1.6, 1.9, and 2.1 mm for mesh sizes of 2, 5, and 8 mm, respectively. Maximum force on the square tube with 3 and 4 mm wall thickness also experienced the same phenomenon as the previous case. A square tube with a thickness of 3 mm has a maximum force of 79.0 kN and is at a displacement of 2.8 mm. When the mesh size increases such as 5 and 8 mm, the maximum force is seen at the displacement of 3.3 and 4.0 mm. This indicates that the displacement magnitude increases by 0.5 and 1.2 mm, respectively. Specimens with 4 mm wall thickness also provide higher displacement on the maximum force when an increase in the mesh size occurred. A 105.9 kN of maximum force is at 3.0 mm displacement when the mesh size is 2 mm. If the mesh size changes to 5 and 8 mm, the maximum force on the displacement increases to 4.5 and 5.2 mm, respectively. This shows that there is a displacement shift of 1.5 and 2.2 mm.

Load *versus* displacement in the case of different materials on the square tube which is mild steel, SAE 1045 steel, and SAE 1008 steel material with two mesh sizes of 5 and 8 mm is shown in Figure 22. As it can be seen that the specimen with mild steel shows a maximum force of approximately 80.3 kN at a displacement of 2.2 and 2.3 mm, respectively. These two displacement values

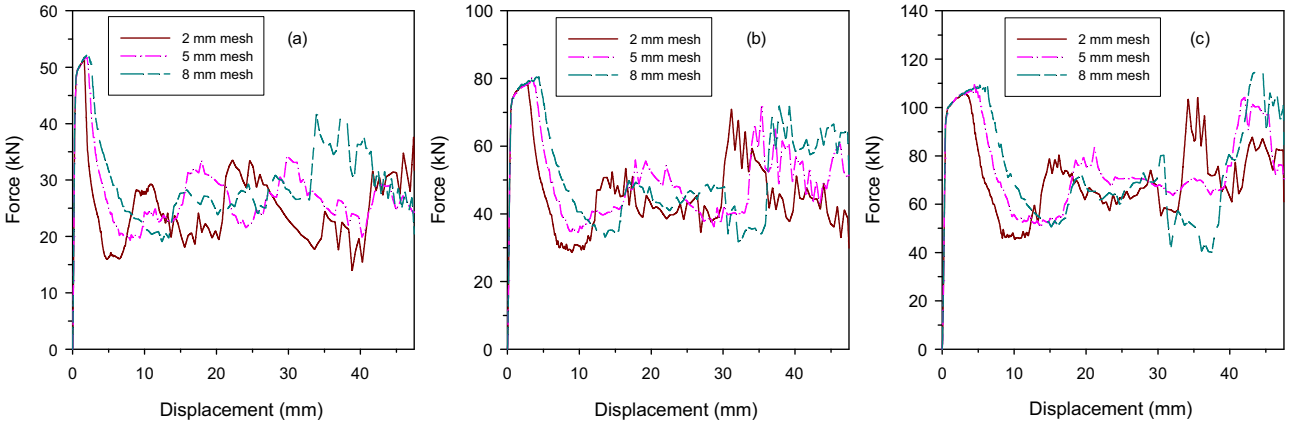

Figure 21: Force *versus* displacement curve with different mesh sizes and three different wall thicknesses. (a) 2 mm, (b) 3 mm, and (c) 4 mm.

are derived from mesh sizes of 5 and 8 mm, respectively. There is an increase that is not large enough by 0.1 mm. The same phenomenon also occurs in specimens with SAE 1008 steel and SAE 1045 steel materials. For a 5 mm mesh size, these two materials produce a maximum force of 80.7 and 161.8 kN, which lies in a displacement of 2.2 and 1.9 mm, respectively. As for the 8 mm mesh size, they occurred at the displacement which is 2.3 and 2.4 mm, respectively. This result indicates that the increase in mesh size from 5 to 5 mm affects the displacement of the maximum force by 0.1 and 0.5 mm, respectively. Details of the effect of mesh on maximum force and displacement are collected in Table 3.

Energy absorption of the specimens with 2, 3, and 4 mm wall thickness and specimens within three different materials depending on the mesh size is shown in Figures 23 and 24. It is observed that the mesh size seems to affect the absorbed energy of the specimen during axial loading. The absorbed energy produces slightly larger values if the mesh size increases as in 2–5 and 5–8 mm. As it is seen, a specimen with 2 mm wall thickness obtained absorbed energy of about 1194.3, 1296.6, and 1,411 J from each 2, 5, and 5 mm mesh size, respectively. This shows an increase of 102.3 and 216.7 J from 2 to 5 mm mesh size. Both specimens of 3 and 4 mm wall thickness show absorbed energy of 2178.2, 2364.4, 2430.1, and 3368.7, 3534.6, and 3504.5 J when mesh size 2, 5, and 8 mm are used, respectively. However, a slightly different phenomenon occurs when the mesh size is 5–8 mm in specimens with 4 mm wall thickness. It seems to have a decrease in value of about 30 J. In all specimens and mesh sizes, only this phenomenon has a decrease in the value of the absorbed energy. The increase in the value of total absorbed energy also occurred in specimens with mild steel, SAE 1045 steel, and SAE 1008 steel as the mesh size increased. For mild steel materials, this increase occurred from the absorbed energy value of 2193.3 to 2273.8 J. While for SAE 1045 steel and SAE 1008 steel, the absorbed energy increased from

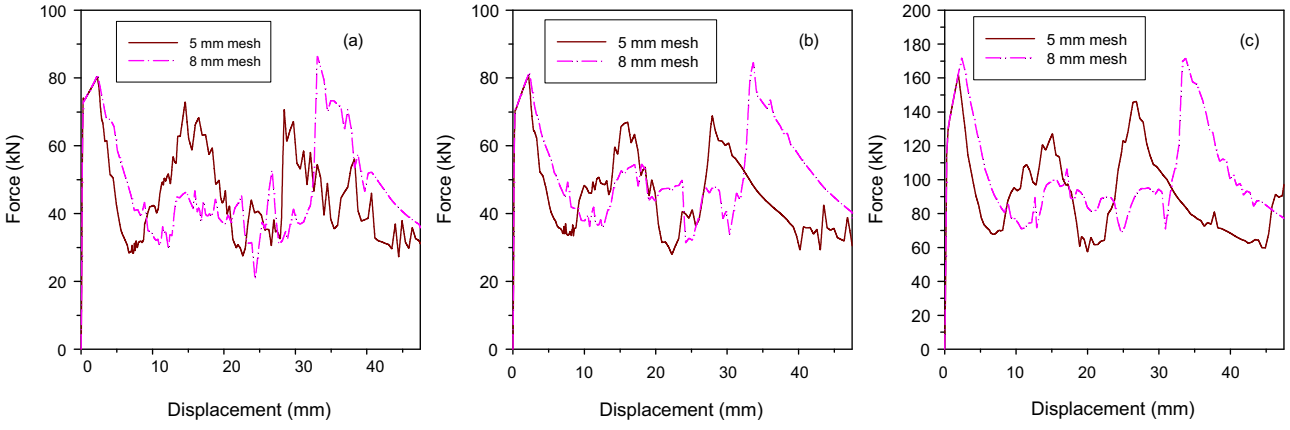

Figure 22: Force *versus* displacement curve with two different mesh sizes and three different steel materials. (a) Mild steel, (b) SAE 1008 steel, and (c) SAE 1045 steel.

Table 3: Maximum force value of the tube under axial loading dependent on the mesh size

Mesh (mm)	Maximum force (kN)						Displacement (mm)					
	Tube wall thickness (mm)			Tube material			Tube wall thickness (mm)			Tube material		
	2	3	4	Mild steel	SAE 1045 steel	SAE 1008 Steel	2	3	4	Mild steel	SAE 1045 steel	SAE 1008 Steel
2	51.6	79.0	105.9	—	—	—	1.6	2.8	3.0	—	—	—
5	51.9	80.2	109.6	80.3	161.8	80.7	1.9	3.3	4.5	2.2	1.9	2.2
8	52.2	80.5	109.2	81.0	171.7	81.6	2.1	4.0	5.2	2.3	2.4	2.3

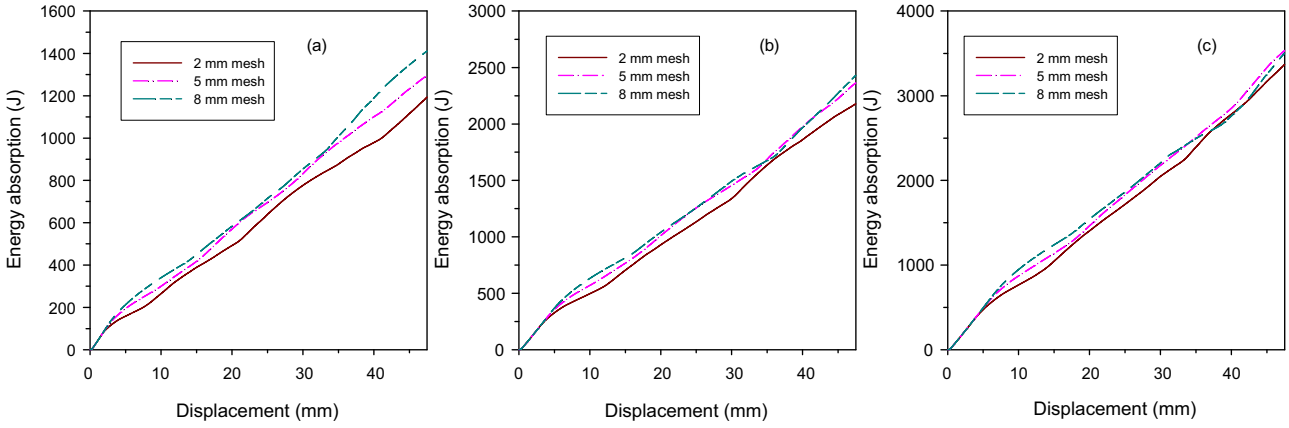

Figure 23: Energy absorption generated during loading from three mesh size with three different wall thicknesses. (a) 2 mm, (b) 3 mm, and (c) 4 mm.

4355.4 to 4823.3 J and 2205.5 to 2453.1 J, respectively. All these phenomena of increasing total absorbed energy occurs when the mesh size is 5–8 mm. It was observed that mesh size 5–8 mm increase at about 3.67, 10.74, and 11.23% of the total energy absorbed on the tube under axial loading for specimens with mild steel, SAE 1045 steel, and SAE 1008 steel material.

Tables 3 and 4 summarize the mesh dependent on the maximum force and total energy absorbed of the tube under axial loading. Specimens with 2 mm wall thickness

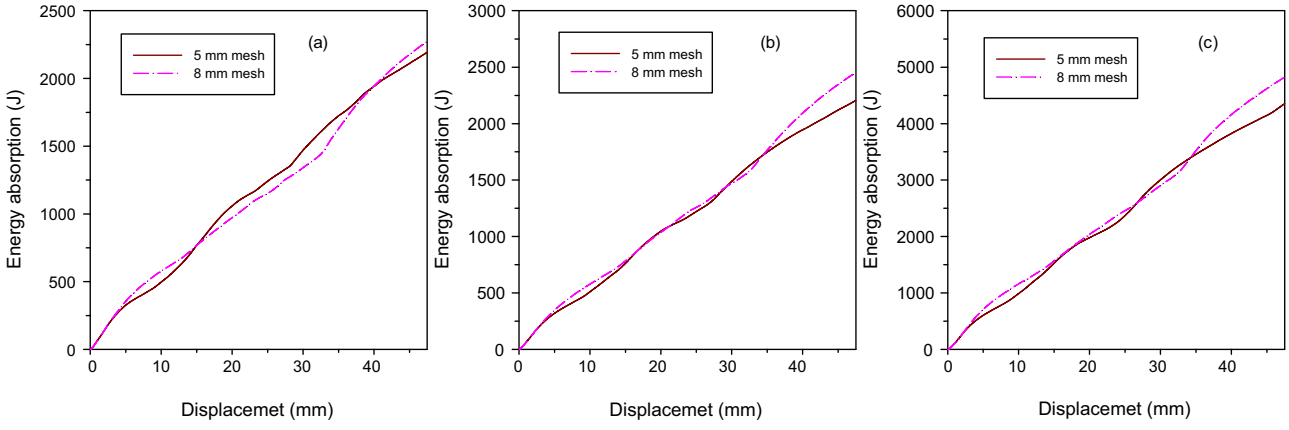

Figure 24: Energy absorption generated during loading from two mesh sizes with three different steel materials. (a) Mild steel, (b) SAE 1008 steel, and (c) SAE 1045 steel.

Table 4: Total energy absorbed value of the tube under axial loading dependent on the mesh size

Mesh size (mm)	Absorbed energy (J)					
	Tube wall thickness (mm)			Tube material		
	2	3	4	Mild steel	SAE 1045 steel	SAE 1008 steel
2	1194.3	2178.2	3368.7	—	—	—
5	1296.6	2364.4	3534.6	2193.3	4355.4	2205.5
8	1,411	2430.1	3504.5	2273.8	4823.3	2453.1

showed the maximum force values, which were approximately the same as 51.6, 51.9, and 52.2 kN for 2, 5, and 8 mm mesh sizes, respectively. Between these three mesh sizes, the percentage difference is not more than 1.15%. As for the 3 and 4 mm specimens, both produce the maximum force of 79.0, 80.2, and 80.5 kN and 105.9, 109.6, and 109.2 kN for 2, 5, and 8 mm mesh sizes, respectively. The percentage difference in the values of the three maximum forces does not exceed 1.88 and 3.43%, respectively.

In a group of specimens with mild steel, SAE 1045 steel, and SAE 1008 steel material, lacking any significant difference occurs in the maximum force values for different mesh sizes. Results for 5 and 8 mm mesh sizes occurred at 80.3 and 81.0 kN for mild steel material. This value has a difference equivalent to 0.7 kN or about 0.87%. SAE 1045 steel and SAE 1008 steel material for the specimen tube also do not have a significant difference (Table 3). However, the highest difference occurs in SAE 1045 steel material, which is 5.94%. The maximum force on SAE 1045 steel material occurs at 161.8 and 171.7 kN for mesh sizes of 5 and 8 mm. Result observations also indicate that specimen with SAE 1008 steel material takes slightly more maximum force with the 8 mm mesh than 5 mm mesh size after axial loading. This is shown by the present value of 81.6 kN maximum force compared to 80.7 kN which has defenses of 1.11% higher.

The mesh-dependent study also shows a quite different value of the total absorbed energy during axial loading for three different thicknesses and materials of the specimens as presented in Table 4. In the case of the wall thickness variation, 2 mm thickness produces a total absorbed energy of about 1194.3 J when 2 mm mesh size is used. Compared to the coarse mesh which is 5 and 8 mm, there is some increase in values of total absorbed energy. It is observed that the percentage increased at approximately 8.57 and 18.14% from the value produced by the 2 mm mesh size. A quite small increase in the total absorbed energy of the specimen as the final simulation also seems to present at 3 and 4 mm wall thickness of the specimens. As depicted in Table 4, the total absorbed energies are 2178.2 and 3368.7 J produced by the 2 mm mesh size. Both values were found to be quite increased to 2364.4, 2430.1 J for the 3 mm wall thickness and 3534.6, 3504.5 J for the 4 mm wall thickness obtained by 5 and 8 mm mesh size, respectively. Numerical observations also indicate that on the specimen materials variation with a larger mesh size takes slightly more total absorbed energy than a small mesh size after compression tests. This phenomenon can be seen when the specimens with mild steel, SAE 1045 steel, and SAE 1008 steel material produce total absorbed energy of approximately 2193.3, 4355.4, and 2205.5 J when a 2 mm mesh size is performed. In 8 mm mesh size, those values increase to about 2273.8, 4823.3, and 2453.1 J, which increase about 3.67, 10.74, and 11.23% from 2 mm mesh size, respectively.

4 Discussion

A numerical study of the thin-walled structure of hollow square tubes under different wall thicknesses and materials subjected to axial impact loading has been carried out in this study. The capability of the tube to withstand the load is shown by the graph of load *versus* displacement, the absorption of the energy, and mode deformation, which is presented in Section 3. The numerical results show that the thickness of the tube wall-size seems to affect the strength to withstand axial loads. As the size of the wall thickness increases, its load-bearing strength and energy absorption capability increase. Materials on the tube are also seen to affect the strength to withstand axial loads and the capability to absorb energy.

Numerical results indicate that the wall thickness of the tube has an important role in load-bearing strength. It was also found to affect the total energy absorbed during an axial loading to the tube specimen. Increasing the size of the wall thickness seems to be effective in enhancing both the load-bearing and energy absorption performance. Load *versus* displacement can be used to see the strength of the specimen tube under axial loading. A typical load *versus* displacement curve is shown in

Figure 10. The start of pressing shows where the axial load reaches an initial peak and it can be said that the specimen is holding its maximum load as shown in Figures 10 and 15. It also seems that the load falls sharply after the maximum force has reached and then it fluctuates periodically. These fluctuations are a result of the formation of the successive folding; each subsequent peak corresponds to the onset of a folding process as depicted in Figures 13 and 14. This phenomenon that the folding process is related to the fluctuation of the force has also been evident in the case of the tube under axial loading carried out by Salehghaffari *et al.* [11]. Lu and Yu [32] also showed the same thing that this force fluctuation is caused by the formation of the successive folding. As it was observed in this study, aluminum specimens from tubes showed that the resistance to axial loads increased by 54.53% from a wall thickness of 2–3 mm, and increased by 36.53% from a wall thickness of 3–4 mm (Figure 12). However, in the case of the material used on the tube, specimens with SAE 1045 steel material seem to have the maximum force higher than the mild steel and SAE 1008 steel material. It has approximately 161.8 kN of maximum force compared with 80.3 and 80.7 kN, which are produced by a specimen with mild steel and SAE 1008 steel material, respectively. SAE 1045 steel material increases the amount of maximum force by 101.49 and 100.49% compared to the mild steel and SAE 1008 material. Thin-walled structures are usually required to withstand certain strength and stiffness under specified loads. Some materials have different properties such as density, Young's modulus, tensile strength, and also failure strain [33]. Material selection is an important thing in the formation of a structural design because it can affect the strength of the structure.

Comparison relating the absorbed energy generated during the axial loading processes of the square tube specimens has been presented. Numerical results show that tube wall thickness can affect the total absorbed energy in the specimen tube under axial loading. At the end of the simulation, the largest wall thickness, which is 4 mm, produces quite a lot of absorbed energy compared to the thickness of 2 and 3 mm; an 82.35% increase in absorbed energy for a 2 mm thickness to 3 mm thickness specimen, and a 49.49% increase for a 3 to 4 mm thickness specimen (Figure 12). Material effects can also affect the total absorbed energy. It is shown that the total energy absorbed from the SAE 1045 material tube is approximately 4355.4 J, which is compared to mild steel and SAE 1008 steel material which is 2193.3 and 2205.5 J, respectively. This indicates that there is an increase in the total energy absorbed, which is almost double in value or about 98.58 and 97.48%. This study indicated that structural design and materials can affect the total absorbed energy. The previous study conducted by Beytüt *et al.* [34] found that the crashworthiness of a spot-welded and double-hat elliptical thin-walled tube can be assessed with the absorbed energy capability. However, Prabowo *et al.* [35] also found that not only the structural design and material that have an effect on the total absorbed energy but also the angle of the load that applies to the structural design.

In the finite element method, a large structure model that examination will divide into small pieces that are called finite elements. Those elements connect all characteristic points that lie in their circumference (the nodes). A mesh is made up of elements that contain nodes that represent the shape of the structure. If the design is very complex and large, the division of this mesh also needs to be considered, whether the size can represent the structure. Therefore, it is very important to choose the right size for this finite element method. Previous research stated that the mesh size can give different results in the simulation results. For example, Prabowo *et al.* [33] found that mesh size also affects how fractures are formed in a structure, *i.e.*, tensile specimens occur from the start until failure occurs. Even the mesh is also associated with a failure criterion, which is implemented on the finite element [33]. This study also shows that different mesh results produce different maximum force and displacement for tube under axial loading. Although the difference is not that noticeable, when the maximum force on a square tube with 2 mm wall thickness is at a displacement of 1.6, 1.9, 2.1 mm for mesh sizes of 2, 5, and 8 mm, respectively. This shows that there is a shift in the position of the maximum force that occurs. Unfortunately, smaller mesh sizes such as 1 mm were not used in this study due to limited computational tools. The small mesh size causes the simulation time to take longer because the computer integrates more into this mesh. Mesh that is too large causes the simulation process to be fast, but the results are also not very accurate. Therefore, it is important to consider the mesh size when using finite elements.

There are still some limitations to the study with this finite element calculation, where geometrical imperfections are not one of the topics of discussion. The test specimen, which is the hollow tube, is also made in a homogeneous model. However, the topic of this discussion will be one of the important studies that will be carried out in future research.

5 Conclusion

This study focuses on how the square tube and the materials can be best designed to strengthen the tube and

absorb the energy during axial loading. Understanding energy absorption of square tubes and materials is important in calculating the damage to structures caused by accidental load, collision, or even an impact. Increasing the wall thickness of the tube leads to increasing the capability to resist loading. Aluminum specimens from tubes showed that the resistance to axial loads increased by 54.53% from a wall thickness of 2–3 mm, and increased by 36.53% from a wall thickness of 3–4 mm. Furthermore, SAE 1045 steel material seems also to have the maximum force higher than the mild steel and SAE 1008 steel material, which approximately increase the strength by 101.49 and 100.49%, respectively. Mesh sensitivity also shows different results for load *versus* displacement as well as the absorbed energy. However, this mesh is only performed on sizes of 2, 5, and 8 mm and is not carried out on refined mesh sizes, for example, 1 mm due to limited computational tools. And also, geometrical imperfections are not one of the topics of discussion in this study. Therefore, future research is needed to overcome these limitations.

Funding information: The authors state no funding involved.

Author contributions: All authors have accepted responsibility for the entire content of this manuscript and approved its submission.

Conflict of interest: The authors state no conflict of interest.

References

[1] Ridwan R, Putranto T, Laksono FB, Prabowo AR. Fracture and damage to the material accounting for transportation crash and accident. Proc Struct Integr. 2020;27:38–45.

[2] Alkhatib SE, Matar MS, Tarlochan F, Laban O, Mohamed AS, Alqwasmi N. Deformation modes and crashworthiness energy absorption of sinusoidally corrugated tubes manufactured by direct metal laser sintering. Eng Struct. 2019;201:109838.

[3] Prabowo AR, Sohn JM, Bae DM, Cho JH. Performance assessment on a variety of double side structure during collision interaction with other ship. Curved Layer Struct. 2017;4:255–71.

[4] Prabowo AR, Bae DM, Sohn JM, Zakki AF, Cao B, Cho JH. Effects of the rebounding of a striking ship on structural crashworthiness during ship-ship collision. Thin-Walled Struct. 2017;115:225–39.

[5] Prabowo AR, Laksono FB, Sohn JM. Investigation of structural performance subjected to impact loading using finite element approach: Case of ship-container collision. Curved Layer Struct. 2020;7:17–28.

[6] Ehlers S, Broekhuijsen J, Alsos HS, Biehl F, Tabri K. Simulating the collision response of ship side structures: A failure criteria benchmark study. Int Shipbuild Prog. 2008;55:127–44.

[7] Izzi MI, Montemurro M, Catapano A, Fanteria D, Pailhès J. Multiscale optimisation of thin-walled structures by considering a global/local modeling approach. Proc Inst Mech Eng Part G J Aerosp Eng. 2021;235:171–88.

[8] Karagiozova D, Nurick GN, Chung Kim Yuen S. Energy absorption of aluminium alloy circular and square tubes under an axial explosive load. Thin-Walled Struct. 2005;43:956–82.

[9] Marzbanrad J, Mehdikhanlo M, Saeedi Pour A. An energy absorption comparison of square, circular, and elliptic steel and aluminum tubes under impact loading. Turkish J Eng Env Sci. 2009;33:159–66.

[10] Guler MA, Cerit ME, Bayram B, Gerçeker B, Karakaya E. The effect of geometrical parameters on the energy absorption characteristics of thin-walled structures under axial impact loading. Int J Crashworthiness. 2010;15:377–90.

[11] Salehghaffari S, Tajdari M, Panahi M, Mokhtarnezhad F. Attempts to improve energy absorption characteristics of circular metal tubes subjected to axial loading. Thin-Walled Struct. 2010;48:379–90.

[12] Tanlak N, Sonmez FO. Optimal shape design of thin-walled tubes under high-velocity axial impact loads. Thin-Walled Struct. 2014;84:302–12.

[13] Kamal M, Shah M, Ahmad N, Wani OI, Sahari J. Study of crashworthiness behavior of thin-walled tube under axial loading by using computational mechanics. Int J Mater Metall Eng. 2016;10:1170–5.

[14] Djerrad A, Fan F, Zhi X, Wu Q. Experimental and FEM analysis of AFRP strengthened short and long steel tube under axial compression. Thin-Walled Struct. 2019;139:9–23.

[15] Abdullah KA, Mohamed Ali JS, Aminanda Y. Experimental and numerical simulation of hollow structure under compression loading. Adv Mater Res. 2012;576:651–4.

[16] ANSYS. ANSYS LS-DYNA User's Guide. Pennsylvania, US: ANSYS, Inc; 2020.

[17] Cabezas EE, Celentano DJ. Experimental and numerical analysis of the tensile test using sheet specimens. Finite Elem Anal Des. 2004;40:555–75.

[18] Ridwan R, Prabowo AR, Muhayat N, Putranto T, Sohn JM. Tensile analysis and assessment of carbon and alloy steels using FE approach as an idealization of material fractures under collision and grounding. Curved Layer Struct. 2020;7:188–98.

[19] Calle MAG, Oshiro RE, Alves M. Ship collision and grounding: Scaled experiments and numerical analysis. Int J Impact Eng. 2017;103:195–210.

[20] Calle MAG, Verleysen P, Alves M. Benchmark study of failure criteria for ship collision modeling using purpose-designed tensile specimen geometries. Mar Struct. 2017;53:68–85.

[21] Storheim M, Amdahl J, Martens I. On the accuracy of fracture estimation in collision analysis of ship and offshore structures. Mar Struct. 2015;44:254–87.

[22] Vu-Bac N, Duong TX, Lahmer T, Zhuang X, Sauer RA, Park HS, et al. A NURBS-based inverse analysis for reconstruction of nonlinear deformations of thin shell structures. Comput Methods Appl Mech Eng. 2018;331:427–55.

[23] Weeger O, Yeung SK, Dunn ML. Isogeometric collocation methods for Cosserat rods and rod structures. Comput Methods Appl Mech Eng. 2017;316:1157–78.

[24] Areias P, Rabczuk T, Msekh MA. Phase-field analysis of finite-strain plates and shells including element subdivision. Comput Methods Appl Mech Eng. 2016;312(C):322–50.

[25] Samaniego E, Anitescu C, Goswami S, Nguyen-Thanh VM, Guo H, Hamdia K, et al. An energy approach to the solution of partial

differential equations in computational mechanics via machine learning: Concepts, implementation and applications. Comput Methods Appl Mech Eng. 2020;362:112790.
[26] Rabczuk T, Areias PM, Belytschko T. A meshfree thin shell method for non-linear dynamic fracture. Int J Numer Methods Eng. 2007;72:524–48.
[27] Rabczuk T, Belytschko T. Cracking particles: A simplified meshfree method for arbitrary evolving cracks. Int J Numer Methods Eng. 2004;61:2316–43.
[28] Vaughan H. The Tearing and Cutting of Mild Steel Plate with Application to Ship Grounding Damage. In: Miller KJ, editors. SMITH RFBT-MB of M. Pergamon; 1980. p. 479–87.
[29] Peterson ML. Steel selection for offshore structures. J Pet Technol. 1975;27:274–82.
[30] Almaraz GMD, Vilchez JAR, Dominguez A. Ultrasonic fatigue on the automotive steels: AISI/SAE 4140T and 1045. Procedia Struct Integr. 2019;18:594–9.
[31] Wang Z, Hu Z, Liu K, Chen G. Application of a material model based on the Johnson-Cook and Gurson-Tvergaard-Needleman model in ship collision and grounding simulations. Ocean Eng. 2020;205:106768.
[32] Lu G, Yu T. Energy absorption of structures and materials. Sawston, UK: Woodhead Publishing; 2003.
[33] Prabowo AR, Ridwan R, Tuswan T, Sohn JM, Surojo E, Imaduddin F. Effect of the selected parameters in idealizing material failures under tensile loads: Benchmarks for damage analysis on thin-walled structures. Curved Layer Struct. 2022;9:258–85.
[34] Beytüt H, Karagöz S, Özel S. Effect of forming history on crashworthiness of a spot-welded and double-hat elliptical thin-walled tube. Eur J Tech. 2019;34(9):275–85.
[35] Prabowo AR, Sohn JM, Bae DM, Setiyawan A. Crashworthiness assessment of thin-walled bottom structures during powered-hard grounding accidents. Proc Int Conf Offshore Mech Arct Eng – OMAE. 2018;11B:77492.